BMC Medical Imaging

RESEARCH

Open Access

# Development of a non-contrast CT-based radiomics nomogram for early prediction of delayed cerebral ischemia in aneurysmal subarachnoid hemorrhage

Lingxu Chen[1], Xiaochen Wang[1], Sihui Wang[1], Xuening Zhao[1], Ying Yan[1], Mengyuan Yuan[1] and Shengjun Sun[1,2*]

## Abstract

**Backgrounds** Delayed cerebral ischemia (DCI) is a significant complication following aneurysmal subarachnoid hemorrhage (aSAH), leading to poor prognosis and high mortality. This study developed a non-contrast CT (NCCT)-based radiomics nomogram for early DCI prediction in aSAH patients.

**Methods** Three hundred seventy-seven aSAH patients were included in this retrospective study. Radiomic features from the baseline CTs were extracted using PyRadiomics. Feature selection was conducted using t-tests, Pearson correlation, and Lasso regression to identify those features most closely associated with DCI. Multivariable logistic regression was used to identify independent clinical and demographic risk factors. Eight machine learning algorithms were applied to construct radiomics-only and radiomics-clinical fusion nomogram models.

**Results** The nomogram integrated the radscore and three clinically significant parameters (aneurysm and aneurysm treatment and admission Hunt-Hess score), with the Support Vector Machine model yielding the highest performance in the validation set. The radiomics model and nomogram produced AUCs of 0.696 (95% CI: 0.578–0.815) and 0.831 (95% CI: 0.739–0.923), respectively. The nomogram achieved an accuracy of 0.775, a sensitivity of 0.750, a specificity of 0.795, and an F1 score of 0.750.

**Conclusion** The NCCT-based radiomics nomogram demonstrated high predictive performance for DCI in aSAH patients, providing a valuable tool for early DCI identification and formulating appropriate treatment strategies.

**Clinical trial number** Not applicable.

**Keywords** Aneurysmal subarachnoid hemorrhage, Delayed cerebral ischemia, Radiomics, Nomogram, Computed tomography

*Correspondence:
Shengjun Sun
sunshengjun0212@163.com
[1]Department of Radiology, Beijing Tiantan Hospital, Capital Medical University, No.119, South Fourth Ring West Road, Fengtai District, Beijing 100070, P.R. China
[2]Department of Radiology, Beijing Neurosurgical Institute, No.119, South Fourth Ring West Road, Fengtai District, Beijing 100070, P.R. China

## Introduction

Aneurysmal subarachnoid hemorrhage (aSAH) is a severe cerebrovascular disease associated with substantial morbidity and mortality [1–3]. Delayed cerebral ischemia (DCI) is among the most prevalent and severe complications of aSAH, affecting approximately 30% of patients and significantly adversely influencing clinical outcomes [4]. The development of DCI typically results in neurological deterioration, increasing the risk of disability and death [5]. Therefore, early, accurate prediction of DCI risk is critical for timely intervention and improving patient prognoses.

Non-contrast computed tomography (NCCT) is the fastest and most convenient imaging modality available for the initial assessment of aSAH patients [6]. Semi-quantitative scales, such as the Hijdra and modified Fisher scores, measure the extent of subarachnoid hemorrhage (SAH) distribution, as well as the presence of intraparenchymal hemorrhage (IPH) or intraventricular hemorrhage (IVH), and are used to predict the risk of DCI [7–9]. However, the predictive accuracy and generalizability of these scoring systems remain limited. In addition, various clinical factors, such as a poor result on a neurological examination (e.g., a high World Federation of Neurosurgical Societies (WFNS) grade), a large amount of subarachnoid and intraventricular blood, large aneurysm size, smoking, hyperglycemia, hydrocephalus, pre-existing diabetes, and female gender, have been identified as predictors of DCI [10, 11].

Radiomics, an emerging imaging analysis technique, has provided a new direction for disease diagnosis and complication prediction by extracting high-dimensional quantitative features from medical images [12, 13]. Radiomics captures texture, shape, and gray-level distribution information within regions of interest, revealing underlying pathophysiological changes [14, 15]. In the context of SAH, radiomics has been utilized for complication predictions and the identification of multiple aneurysms [16, 17]. However, more research is needed on applying NCCT-based radiomic features to the early prediction of DCI.

Machine learning algorithms, including support vector machines, random forests, and neural networks, have displayed considerable potential in the analysis of radiomic features and complex pattern recognition [18, 19]. These algorithms capture the nonlinear relationships between imaging features and clinical outcomes, thereby improving model performance [20, 21]. By integrating radiomic features with clinical variables, machine learning-based nomograms offer personalized risk assessments that support clinical decision-making [22, 23].

The main objective of this study was to accurately predict the complication of SAH using radiomic features extracted from NCCT scans and machine learning algorithms. We constructed radiomics-only and radiomics-clinical fusion nomogram models using machine learning algorithms to predict the risk of DCI in aSAH patients. The nomograms could improve early detection of high-risk DCI patients, facilitate personalized treatment management, and improve patient outcomes.

## Methods

### Patient selection

This study was approved by the Institutional Review Board (IRB) of Beijing Tiantan Hospital, Capital Medical University (KY2022-058-02). The IRB waived the need for informed consent forms. A total of 371 patients newly diagnosed with subarachnoid hemorrhage (SAH) from Beijing Tiantan Hospital between August 2017 and September 2023 were included in the analysis. All patients underwent non-contrast CT (NCCT) within 24 h after symptom onset. The inclusion criteria were as follows: (1) spontaneous SAH confirmed by head CT or lumbar puncture upon admission; (2) intracranial aneurysm confirmed as the source of bleeding by digital subtraction angiography (DSA) or surgery; (3) complete baseline thick-slice NCCT images and clinical data were obtained; and (4) all patients underwent endovascular coiling or surgical clipping of the responsible aneurysm after CT imaging. Exclusion criteria were: (1) patients experienced intracranial hemorrhage due to other reasons (e.g., trauma, hypertensive cerebral hemorrhage, vascular malformation, or tumor-related stroke); (2) had a history of intracranial surgery; (3) CT images presented significant motion or artifact distortions; and (4) brain parenchymal hemorrhage that extended into the subarachnoid space. Eligible patients were randomly assigned to a training set or an internal validation set at a ratio of 8:2. The flow chart for patient enrollment is displayed in Fig. 1, showing the initial pool of 504 patients and the 377 included in the study.

### CT scans

CT scans were obtained using three different scanners across 377 cases. A Philips iCT 256 (Philips Healthcare, Best, the Netherlands), used for 138 cases; a GE LightSpeed VCT (GE Healthcare, Chicago, IL, USA) was used for 110 case; a GE Revolution CT (GE Healthcare, Chicago, IL, USA) was used for 129 cases. All scans were performed with a slice thickness of 5 mm and a section interval of 5 mm. The number of slices and field of view (FOV) were adjusted according to patient size, ensuring coverage from the skull base to the vertex. As a result, 32 slices were acquired in 298 cases, and 28 slices in 73 cases. Scanning parameters included tube voltages of 120 kVp for the Philips iCT 256, 120 kVp for the GE LightSpeed VCT, and 120 kVp for the GE Revolution CT. The

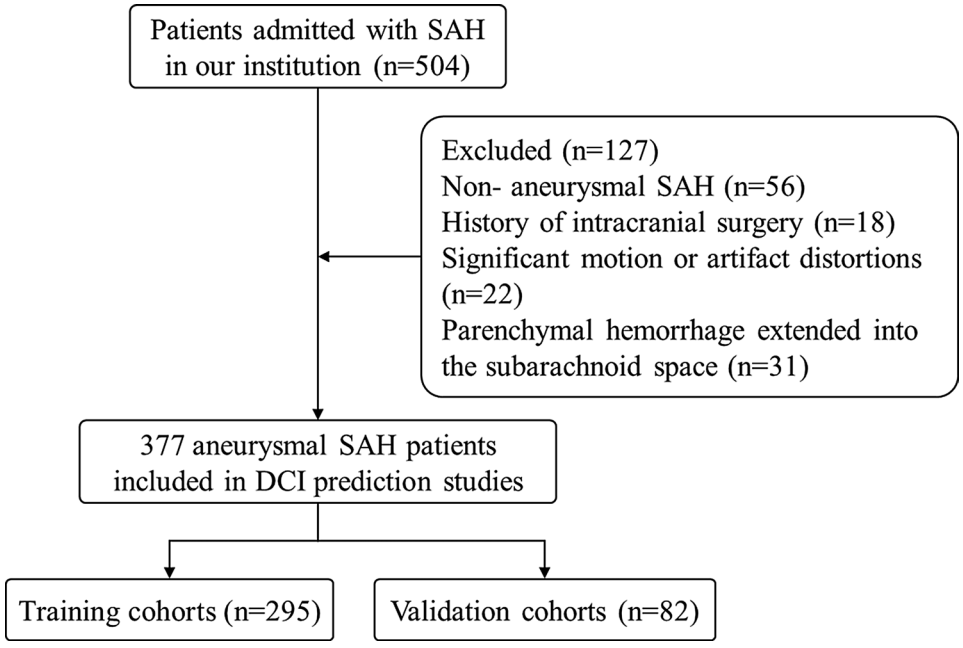


**Fig. 1** The flowchart of the study population. DCI: Delayed cerebral ischemia; aSAH: aneurysmal subarachnoid haemorrhage

tube current settings were 360 mA for the Philips iCT 256, 150 mA for the GE LightSpeed VCT, and 283 mA for the GE Revolution CT.

All NCCT scans were converted to the Neuroimaging Informatics Technology Initiative (NIfTI) format to standardize the data for analysis. Skull stripping was performed, and the window width and level were adjusted to 90 and 42, respectively. The images and corresponding labels were resized to 88, 88, and 32 to ensure uniformity across the dataset.

#### Lesion segmentation

Baseline and 24-hour follow-up CT images were saved as DICOM files using the Picture Archiving and Communication System (PACS). We used an automated segmentation model to reduce the workload and avoid inter-observer variability in the manual hemorrhage region delineation. The model was based on the U-Net + + architecture, implemented in the NeuBrainCare software developed by Neusoft Medical Systems to automatically segment subarachnoid hemorrhage (SAH) regions of interest (ROIs). The ROIs for sulcal and cisternal blood were labelled mask 1, while the ROI for ventricular blood was labelled mask 2. This was undertaken to identify the significant features for outcome prediction based on hemorrhage at different locations. Mask 2 was assigned a value of zero for samples without intraventricular hemorrhage. Comparisons between Automated Segmentation and Hemorrhage Segmentation were conducted by a senior radiologist with over ten years of head CT interpretation experience, as shown in Fig. 2.

#### Clinical data

The clinical characteristics of the participants are detailed in Table 1. Data were sourced from the patients' medical records, and all variables were baseline data collected prior to surgical intervention. Variables included age, gender, surgical approach, aneurysm location, systolic blood pressure (SBP), level of consciousness (LOC), hypertension, diabetes, smoking, alcohol consumption, Hunt-Hess (HH) score, and modified Rankin Scale (mRS) score. Treatments included surgical clipping and endovascular coiling. The aneurysm locations were classified into anterior and posterior circulations.

#### Delayed cerebral ischemia

The definition and diagnosis of delayed cerebral ischemia (DCI) were based on those established by Vergouwen et al. [4] DCI was defined as (1) new, persistent, or transient focal neurological impairment (e.g., aphasia, apraxia, hemianopia, or neglect) between days four and 14 after aSAH with no other identifiable cause; or (2) a decrease of a minimum of two points on the Glasgow Coma Scale (GCS), which may involve changes in the eye, verbal, or motor response scores, or the overall score, accompanied by new low-density areas on head CTs (not present on admission or immediate post-operative scans). Vasospasm was confirmed as the sole cause of DCI between four and 30 days after SAH. All patients underwent blood pressure management according to standard clinical protocols. This included continuous intravenous infusion of nimodipine at a concentration of 0.2 mg/mL, administered at a rate of 10 mL/h, to maintain systolic blood pressure below 160 mm Hg for ten days. If systolic blood

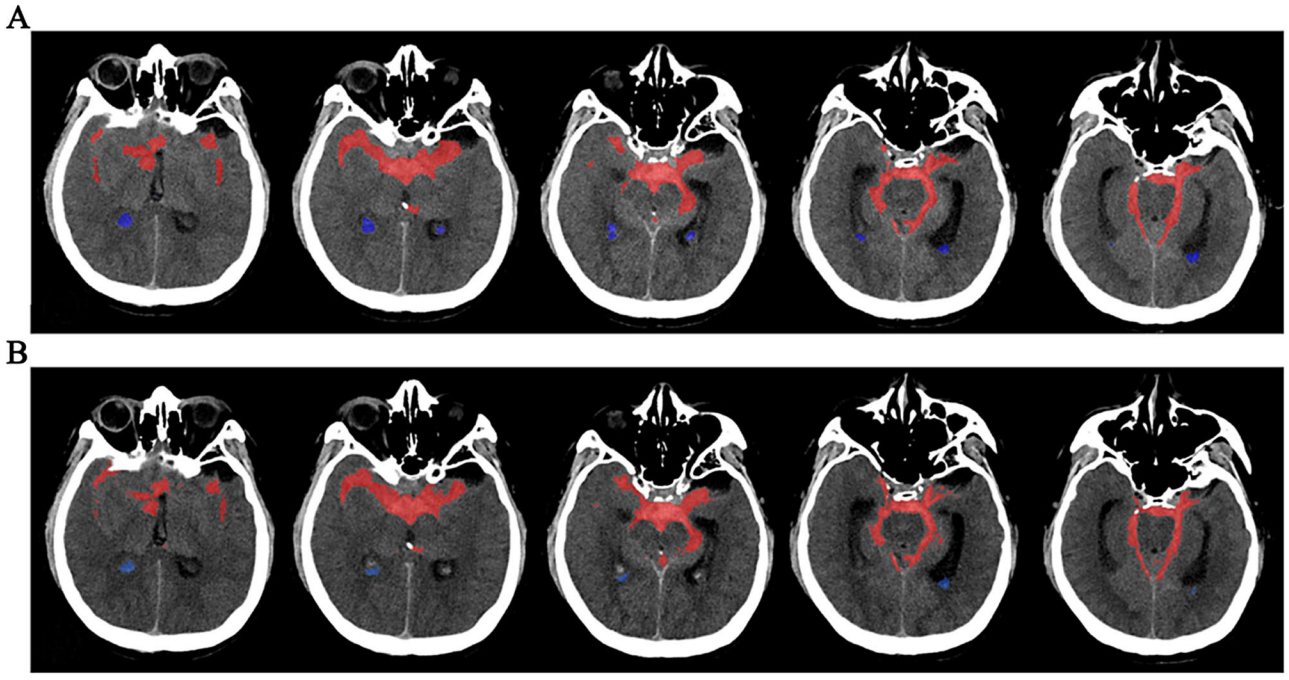


**Fig. 2** Examples of the comparison between manual segmentation and the deep learning segmentation algorithm. **A**. Manual segmentation; **B**. Deep learning segmentation algorithm. The red mask indicates hemorrhage in the sulci and cisterns (mask 1), while the blue mask indicates hemorrhage in the ventricles (mask 2). Using manual segmentation as the gold standard, the dice coefficients of this automatic segmentation for mask 1 and mask 2 are 0.891 and 0.885, respectively

**Table 1** Clinical characteristics of included patients

| Feature name | Training cohort ($n=295$) | | | *p*-value | Internal validation cohort ($n=82$) | | | *p*-value |
|---|---|---|---|---|---|---|---|---|
| | ALL | Non-DCI ($n=158$) | DCI ($n=141$) | | ALL | Non-DCI ($n=44$) | DCI ($n=38$) | |
| Age | 54.73 ± 10.37 | 53.32 ± 10.49 | 56.36 ± 10.02 | 0.035 | 56.10 ± 10.35 | 53.98 ± 11.32 | 58.55 ± 8.60 | 0.045 |
| mRS | 0.14 ± 0.51 | 0.17 ± 0.61 | 0.10 ± 0.35 | 0.547 | 0.32 ± 0.84 | 0.30 ± 0.76 | 0.34 ± 0.94 | 0.809 |
| Gender | | | | 0.792 | | | | 1.00 |
| Women | 210 (71.19) | 114 (72.15) | 96 (70.07) | | 50 (60.98) | 27 (61.36) | 23 (60.53) | |
| Men | 85 (28.81) | 44 (27.85) | 41 (29.93) | | 32 (39.02) | 17 (38.64) | 15 (39.47) | |
| Treatment | | | | < 0.001 | | | | < 0.001 |
| Coiling | 131 (44.41) | 107 (67.72) | 24 (17.52) | | 36 (43.90) | 29 (65.91) | 7 (18.42) | |
| Clipping | 164 (55.59) | 51 (32.28) | 113 (82.48) | | 46 (56.10) | 15 (34.09) | 31 (81.58) | |
| Location | | | | 0.109 | | | | 0.002 |
| Anterior | 230 (77.97) | 117 (74.05) | 113 (82.48) | | 61 (74.39) | 26 (59.09) | 35 (92.11) | |
| Posterior | 65 (22.03) | 41 (25.95) | 24 (17.52) | | 21 (25.61) | 18 (40.91) | 3 (7.89) | |
| Admission SBP ≥ 160 (mm Hg), n (%) | 185 (62.71) | 89 (56.33) | 96 (70.07) | 0.021 | 47 (57.32) | 23 (52.27) | 24 (63.16) | 0.441 |
| LOC | 62 (21.02) | 25 (15.82) | 37 (27.01) | 0.033 | 21 (25.61) | 7 (15.91) | 14 (36.84) | 0.056 |
| Hypertension | 88 (29.83) | 41 (25.95) | 47 (33.33) | 0.204 | 23 (28.05) | 10 (22.73) | 13 (34.21) | 0.326 |
| Diabetes | 19 (6.44) | 8 (5.06) | 11 (8.03) | 0.425 | 8 (9.76) | 3 (6.82) | 5 (13.16) | 0.554 |
| Smoke | 51 (17.29) | 28 (17.72) | 23 (16.79) | 0.955 | 23 (28.05) | 12 (27.27) | 11 (28.95) | 1.0 |
| Alcohol | 40 (13.56) | 22 (13.92) | 18 (13.14) | 0.979 | 16 (19.51) | 7 (15.91) | 9 (23.68) | 0.544 |
| H-H score (3 ~ 5) | 129 (43.73) | 31 (19.62) | 98 (71.53) | < 0.001 | 36 (43.90) | 13 (29.55) | 23 (60.53) | 0.009 |

DCI: Delayed cerebral ischemia; LOC: level of consciousness; SBP: systolic blood pressure

pressure dropped below 110 mm Hg, the infusion rate was reduced to 5 mL/h (Supplementary file).

### Radiomics feature extraction and selection

The code for the radiomic feature extraction was from the "One-key AI" platform (http://www.medai.icu/), which is based on the Python-based PyRadiomics tool. 3,670 morphological, histogram, and texture features were generated from mask 1 and mask 2. Prior to feature selection, the feature values were standardized using Z-score normalization: $z = (x - \mu) / \sigma$, where x represents the original data point, $\mu$ is the feature mean, and $\sigma$ is the standard deviation. This standardization eliminated the impact of different scales or magnitudes across features. Feature selection was performed using t-tests with a P-value threshold of 0.05. Features with Pearson correlation coefficients greater than 0.9 were excluded. Significant, highly correlated features were identified using univariate logistic regression analysis. Finally, based on the maximum area under the curve (AUC) criterion, LASSO regression was applied to the training cohort using 10-fold cross-validation to select an optimal subset of features.

### Radiomics model and nomogram construction

Eight machine learning algorithms Logistic Regression (LR) [24], Multilayer Perceptron (MLP) [25], Support Vector Machine (SVM) [26], Random Forest (RF) [27], Extremely Randomized Trees (Extra Trees, ET), Extreme Gradient Boosting (XGBoost), Light Gradient Boosting Machine (LightGBM), and K-Nearest Neighbors (KNN) [28] were used to build the radiomics models. The optimal model's radscore was selected as the radiomic feature. A nomogram model was created by combining clinical variables of radiological significance with the optimal radiomics model using stepwise multivariable logistic regression analysis. All model parameters were automatically optimized through hyperparameter tuning, and five-fold cross-validation was used during training to assess and iteratively improve the model's performance. The model's diagnostic performance was evaluated using ROC analysis. The models were validated with the internal validation cohort using the same methodology.

### Statistical analysis

Continuous variables in the clinical data were analyzed using independent t-tests or Mann-Whitney U tests, depending on their data distribution. Categorical variables were compared using Chi-square tests. Each variableltion. Categoric variables in the training cohort were determined through univariate logistic regression to identify independent risk factors for DCI. Variables significantly associated with DCI were included in stepwise multivariable logistic regression analysis. To compare the performance of radiomics, clinical models, and the nomogram across various machine learning algorithms, receiver operating characteristic (ROC) curves were calculated for both the training and validation sets of each model. Key performance metrics, including sensitivity, specificity, accuracy, and the area under the ROC curve (AUC), were computed for each model to evaluate and compare their diagnostic effectiveness.

## Results

### Clinical characteristics

The clinical characteristics of the patients are summarized in Table 1. A total of 377 patients were included in the study, of which 175 patients (137 in the training set and 38 in the validation set) developed DCI; 202 patients (158 in the training set and 44 in the validation set) did not develop DCI. No significant differences were observed in baseline clinical data between the training and validation groups. The mean age of the entire cohort was $55.03 \pm 11.13$ years, with patients who developed DCI being older than those who did not ($P = 0.035$ in the training set, $P = 0.045$ in the validation set). Males accounted for 31.03% ($n = 117$) of the population. The surgical approach to aneurysm repair was significantly associated with the occurrence of DCI ($P < 0.001$ in both training and validation cohorts), with patients undergoing surgical clipping exhibiting a higher likelihood of developing DCI compared to those treated with endovascular coiling. Additionally, a systolic blood pressure $\geq 160$ mm Hg upon admission was correlated with an increased risk of DCI in the training cohort ($P = 0.021$). Furthermore, patients presenting with loss of consciousness at admission were more frequently observed to develop DCI ($P = 0.033$ in the training cohort). Univariate and multivariate analyses were conducted in the training cohort. The univariate logistic regression analysis identified location ($P = 0.037$), treatment ($P < 0.001$), and Hunt-Hess score ($P < 0.001$) as independent factors associated with DCI. Multivariable analysis revealed that a Hunt-Hess score of 3–5 (OR: 3.493 [2.203, 5.534]) and location (OR: 0.3, [0.185, 0.486]) were independently associated with DCI. Therefore, these independent risk factors were incorporated into the DCI risk estimation nomogram.

### Radiomics features extraction and machine learning model development

The radiomics workflow is shown in Fig. 3. Radiomics features were extracted separately from the ROI regions of masks 1 and 2 on the NCCT images. A total of 3,670 features were extracted from the NCCT images, with the feature distribution shown in Fig. 4. After using t-tests, Pearson correlation, and LASSO regression for feature selection, 16 features were identified, including ten features from the sulcal and cisternal blood regions (two first-order features, one shape feature, four GLCM

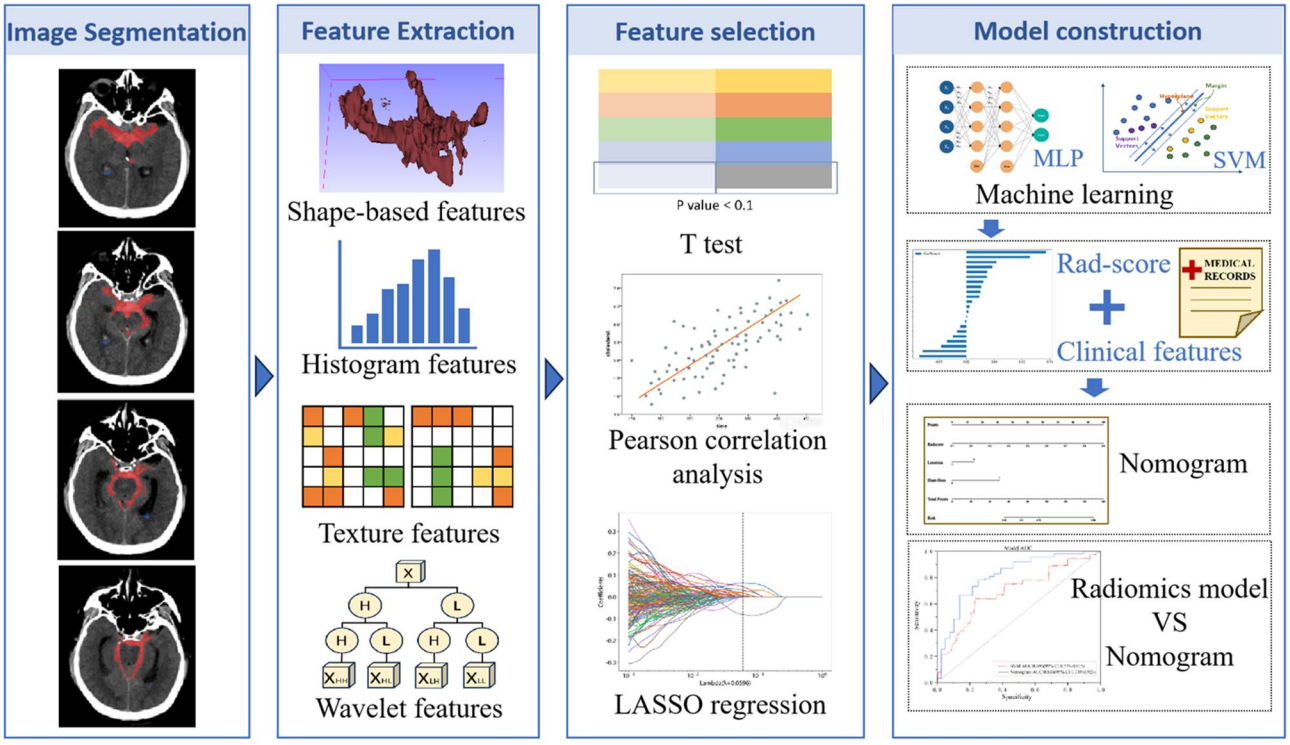


**Fig. 3** Depicts the comprehensive workflow of the radiomics-based machine learning models and the nomogram

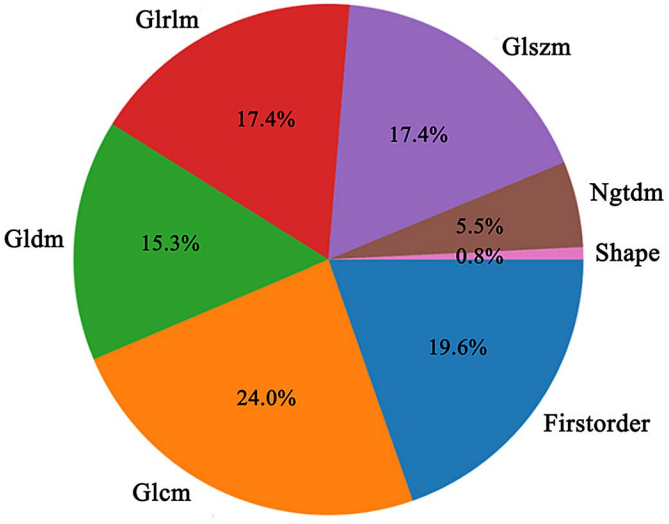


| Features | Count |
|---|---|
| firstorder | 720 |
| glcm | 880 |
| gldm | 560 |
| glrlm | 640 |
| glszm | 640 |
| ngtdm | 200 |
| shape | 28 |

**Fig. 4** Extracted radiomics features. Firstorder: First Order Statistics. glcm: Gray Level Co-occurrence Matrix. gldm: Gray Level Dependence Matrix. glrlm: Gray Level Run Length Matrix. glszm: Gray Level Size Zone Matrix. ngtdm: Neighboring Gray Tone Difference Matrix. shape: Shape-Based Features

features, one GLSZM feature, and two NGTDM features). Six features were selected from the ventricular blood regions (one GLRLM feature, two GLCM features, and three GLSZM features). Using the selected features, DCI prediction models were constructed using the eight machine learning algorithms. Among all models, the SVM model demonstrated the best performance in predicting DCI, with an AUC of 0.696 (95% CI: 0.578–0.815). The accuracy, precision, recall, and F1 score were 0.611, 0.687, 0.611, and 0.647, respectively (Tables 2 and 3). The Radscore generated from the SVM model was selected for subsequent analysis.

### Nomogram development

The Radscore generated from the SVM model was combined with clinically relevant variables, including

**Table 2** The performance of radiomics models constructed using eight machine learning methods in the training sets

| Model_name | Accuracy | AUC | 95% CI | Sensitivity | Specificity | PPV | NPV | Precision | Recall | F1 | Threshold | Task |
|---|---|---|---|---|---|---|---|---|---|---|---|---|
| LR | 0.708 | 0.737 | 0.6792–0.7947 | 0.590 | 0.809 | 0.725 | 0.698 | 0.725 | 0.590 | 0.650 | 0.530 | label-train |
| SVM | 0.739 | 0.804 | 0.7540–0.8540 | 0.604 | 0.854 | 0.779 | 0.717 | 0.779 | 0.604 | 0.681 | 0.568 | label-train |
| KNN | 0.715 | 0.843 | 0.8007–0.8850 | 0.433 | 0.955 | 0.892 | 0.664 | 0.892 | 0.433 | 0.583 | 0.600 | label-train |
| RandomForest | 0.756 | 0.821 | 0.7735–0.8686 | 0.709 | 0.796 | 0.748 | 0.762 | 0.748 | 0.709 | 0.728 | 0.455 | label-train |
| ExtraTrees | 0.698 | 0.752 | 0.6951–0.8080 | 0.657 | 0.732 | 0.677 | 0.714 | 0.677 | 0.657 | 0.667 | 0.451 | label-train |
| XGBoost | 0.842 | 0.925 | 0.8957–0.9535 | 0.918 | 0.777 | 0.778 | 0.917 | 0.778 | 0.918 | 0.842 | 0.363 | label-train |
| LightGBM | 0.766 | 0.843 | 0.7989–0.8871 | 0.694 | 0.828 | 0.775 | 0.760 | 0.775 | 0.694 | 0.732 | 0.489 | label-train |
| MLP | 0.718 | 0.749 | 0.6918–0.8057 | 0.590 | 0.828 | 0.745 | 0.703 | 0.745 | 0.590 | 0.658 | 0.539 | label-train |

AUC: Area Under the Curve, 95% CI: 95% Confidence Interval, PPV: Positive Predictive Value, NPV: Negative Predictive Value, F1: F1 Score

**Table 3** The performance of radiomics models constructed using eight machine learning methods in the validation sets

| Model_name | Accuracy | AUC | 95% CI | Sensitivity | Specificity | PPV | NPV | Precision | Recall | F1 | Threshold | Task |
|---|---|---|---|---|---|---|---|---|---|---|---|---|
| LR | 0.675 | 0.689 | 0.5703–0.8085 | 0.556 | 0.773 | 0.667 | 0.680 | 0.667 | 0.556 | 0.606 | 0.535 | label-val |
| SVM | 0.700 | 0.696 | 0.5777–0.8150 | 0.611 | 0.773 | 0.687 | 0.708 | 0.687 | 0.611 | 0.647 | 0.508 | label-val |
| KNN | 0.625 | 0.621 | 0.4963–0.7449 | 0.222 | 0.955 | 0.800 | 0.600 | 0.800 | 0.222 | 0.348 | 0.600 | label-val |
| RandomForest | 0.637 | 0.653 | 0.5308–0.7760 | 0.500 | 0.750 | 0.621 | 0.647 | 0.621 | 0.500 | 0.554 | 0.508 | label-val |
| ExtraTrees | 0.675 | 0.694 | 0.5763–0.8119 | 0.583 | 0.750 | 0.656 | 0.687 | 0.656 | 0.583 | 0.618 | 0.473 | label-val |
| XGBoost | 0.637 | 0.634 | 0.5105–0.7584 | 0.222 | 0.977 | 0.889 | 0.606 | 0.889 | 0.222 | 0.356 | 0.779 | label-val |
| LightGBM | 0.637 | 0.654 | 0.5318–0.7769 | 0.583 | 0.682 | 0.600 | 0.667 | 0.600 | 0.583 | 0.592 | 0.494 | label-val |
| MLP | 0.675 | 0.685 | 0.5652–0.8048 | 0.556 | 0.773 | 0.667 | 0.680 | 0.667 | 0.556 | 0.606 | 0.535 | label-val |

AUC: Area Under the Curve, 95% CI: 95% Confidence Interval, PPV: Positive Predictive Value, NPV: Negative Predictive Value, F1: F1 Score

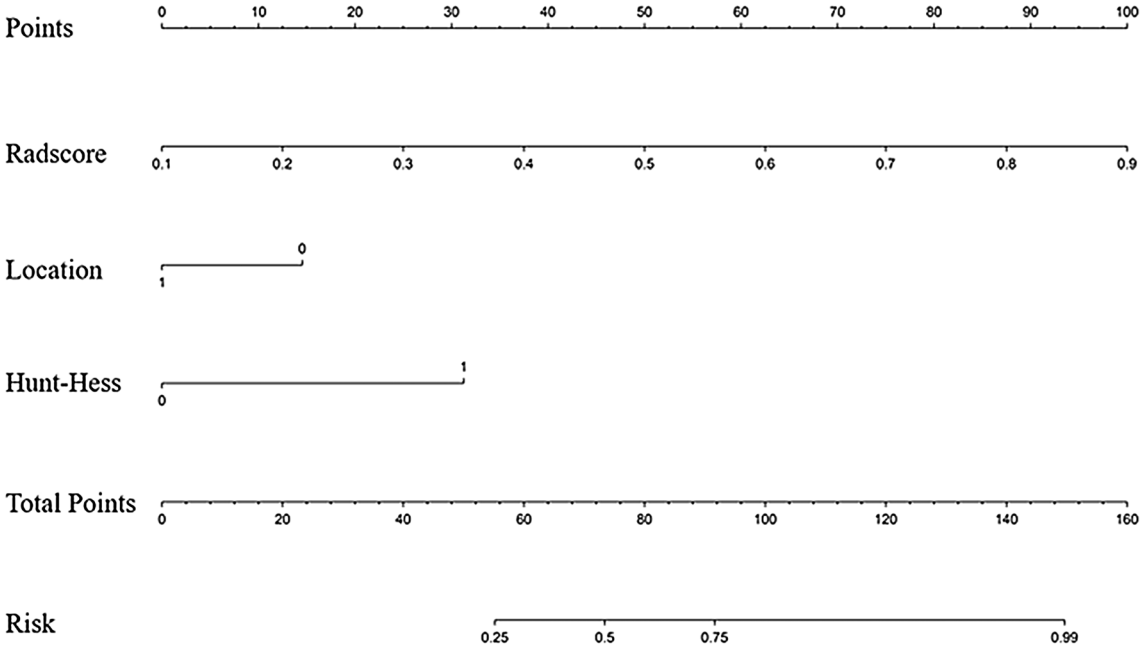


**Fig. 5** The nomogram for predicting DCI in aSAH patients. The nomogram integrates radscore from the radiomics SVM model, aneurysm location, and Hunt-Hess score. Each variable is assigned a point value based on its contribution to the risk prediction model. The total points correspond to the overall risk of DCI, which is indicated on the risk axis. Higher total points reflect a higher risk of developing DCI. SVM: Support Vector Machine; DCI: Delayed cerebral ischemia; aSAH: aneurysmal subarachnoid haemorrhage

aneurysm location and the admission Hunt-Hess score, to construct the nomogram (Fig. 5). This nomogram achieved an accuracy of 0.775, a sensitivity of 0.750, a specificity of 0.795, and an F1 score of 0.750 in predicting DCI (Table 4). The nomogram's AUC (0.831, 95% CI: 0.739–0.923) was higher than the SVM radiomics model alone (Fig. 6).

## Discussion

We developed a predictive nomogram for delayed cerebral ischemia in aneurysmal subarachnoid hemorrhage patients by integrating radiomics features and clinical data. Using a deep learning-based approach for automated segmentation and radiomics feature extraction from NCCT scans, combined with clinical variables, we constructed a robust model that significantly improved DCI prediction. The results demonstrated that our model provides valuable prognostic information for identifying high-risk patients, potentially enhancing clinical decision-making.

The timely prediction of DCI is critical, as interventions must be initiated before ischemia occurs or progresses to irreversible infarction. For instance, nimodipine is the only drug proven to improve outcomes in aSAH patients, and it must be administered within 96 h of SAH onset to be effective [29]. Early prediction allows prompt initiation of treatment, potentially preventing significant morbidity and mortality. NCCT-based prediction methods often rely on semi-quantitative scoring systems, such as the modified Fisher score, Hijdra score, and the Barrow Neurological Institute (BNI) scale [8, 9, 30], which assess the extent of subarachnoid and intraventricular hemorrhage. However, these methods are subject to low reproducibility and interobserver variability in clinical practice. More advanced quantitative assessment methods, such as total SAH volume in various brain regions, have been shown to predict DCI. Studies by Zijlstra et al., Steen et al., and Yuan et al. have applied artificial intelligence to automatically segment and quantify sulcal, cisternal, and ventricular hemorrhages [31–33], with the cisternal hemorrhage volume most robustly associated with DCI.

Radiomics allows for the extraction of high-dimensional quantitative features, such as texture patterns and gray-level distributions, providing more detailed information compared to visual image interpretation [34–36]. Shan et al. demonstrated the effectiveness of radiomics features extracted from NCCT images in predicting outcomes in SAH patients [16]. Studies related to the prediction of DCI by imaging histology are currently very limited; Ramos et al. used an autoencoder to extract image features from CT images and combined them with clinical data to create an ML model that predicted DCI with an AUC of up to:0.74 (95% CI 0.72 to 0.75) [37]. We conducted a radiomics analysis of NCCT features related to hemorrhage, selecting regions of interest (ROIs) based on previous studies, including separate segmentation of sulcal, cisternal, and ventricular hemorrhage. This

**Table 4** Comparison of the performance between the radiomics model constructed using SVM and the nomogram in the training and validation sets

| | Signature | Accuracy | AUC | 95% CI | Sensitivity | Specificity | PPV | NPV | Precision | Recall | F1 | Threshold | Cohort |
|---|---|---|---|---|---|---|---|---|---|---|---|---|---|
| 1 | Radiomics | 0.739 | 0.804 | 0.7540–0.8540 | 0.604 | 0.854 | 0.779 | 0.717 | 0.779 | 0.604 | 0.681 | 0.568 | Train |
| 2 | Nomogram | 0.821 | 0.882 | 0.8425–0.9214 | 0.813 | 0.828 | 0.801 | 0.839 | 0.801 | 0.813 | 0.807 | 0.461 | Train |
| 4 | Radiomics | 0.700 | 0.696 | 0.5777–0.8150 | 0.611 | 0.773 | 0.687 | 0.708 | 0.687 | 0.611 | 0.647 | 0.508 | Validation |
| 5 | Nomogram | 0.775 | 0.831 | 0.7391–0.9225 | 0.750 | 0.795 | 0.750 | 0.795 | 0.750 | 0.750 | 0.750 | 0.503 | Validation |

AUC: Area Under the Curve, 95% CI: 95% Confidence Interval, PPV: Positive Predictive Value, NPV: Negative Predictive Value, F1: F1 Score

approach allowed us to assess the contribution of hemorrhage in different locations to DCI prediction.

Numerous published studies have explored clinical factors related to DCI, including poor neurological status (high WFNS score), smoking, hyperglycemia, hydrocephalus, diabetes, and female sex; machine-learning models based on these clinical features have been constructed previously. For example, Savarraj et al. [38] developed a machine-learning model using 31 clinical and laboratory variables, achieving an AUC of 0.75 (95% CI: 0.64–0.84). Similarly, de Jong et al. [39] utilized a feedforward artificial neural network to predict DCI with an AUC of 0.72, sensitivity of 74%, and specificity of 94%. Our model integrated radiomics scores with easily accessible clinical features such as the Hunt-Hess score, a widely used clinical grading system for assessing the severity of SAH and predict complication. The predictive value of the Hunt-Hess score for DCI aligns with previous research [40, 41]. Additionally, our study associated aneurysm location in the anterior circulation (including the anterior communicating artery, anterior cerebral artery, middle cerebral artery, and their branches) with DCI. We incorporated the aneurysm location in our model based on the gold standard of surgery (endovascular or open surgery). However, in clinical practice, this variable also could be reliably included in early and rapid assessment using preoperative imaging modalities such as CTA, as supported by a previous study [42]. This approach would allow clinicians to more quickly and effectively utilize our nomogram for early DCI risk prediction.

Our study also applied automated hemorrhage segmentation to create masks for different hemorrhage regions, facilitating radiomics feature extraction. Automated segmentation reduces inter-observer variability and offers speed and labor efficiency, which is crucial in emergency scenarios like SAH. Feature weights from traditional radiomics logistic regression and the radscore formula revealed that the squareroot_glcm_correlation and wavelet_HLH_glszm_Small_ Area_High_Gray_Level_Emphasis, extracted from cisternal and sulcal blood, were the most influential features (Fig. 7). Squareroot_glcm_correlation reflects the correlation of gray values between neighboring pixels, with higher values indicating a more uniform texture. This could suggest persistent and diffuse blood accumulation, impairing cerebrospinal fluid circulation and cerebral perfusion, leading to ischemic damage. Wavelet_HLH_ glszm_Small Area_High_Gray_Level_Emphasis focuses on small, high-density areas, such as blood clots in the cisterns, indicating higher local blood density, which could also increase ischemic risk. Additionally, wavelet_LLH_glcm_correlation from ventricular hemorrhage, highlights the correlation between pixel gray values, especially after LLH wavelet transformation, suggesting more homogeneous blood

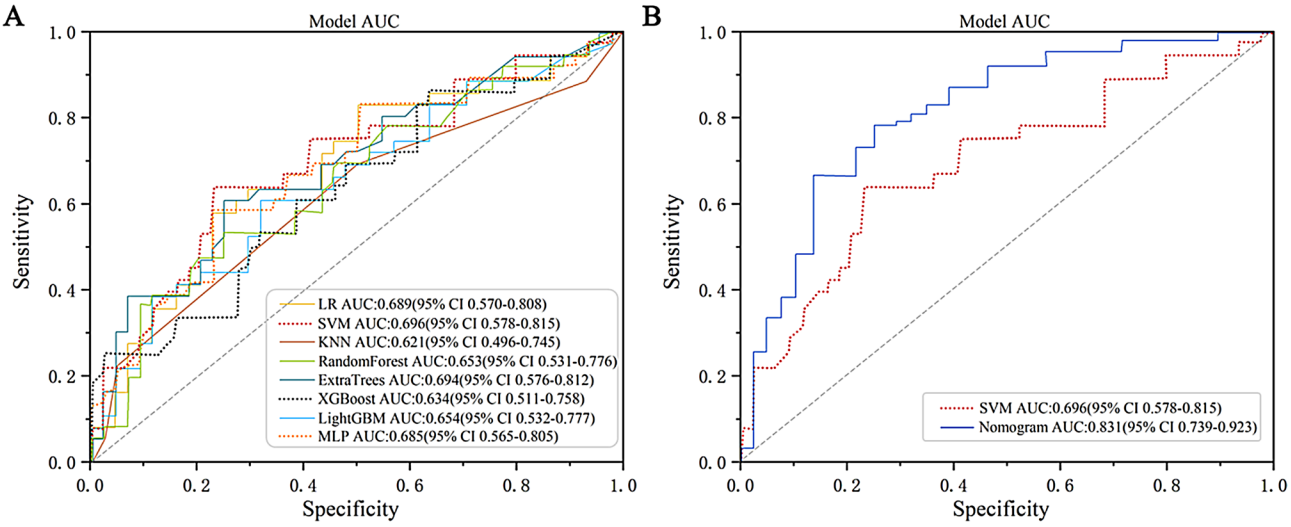


**Fig. 6** AUC of the model. **A**. Shows the radiomics models constructed using eight machine learning methods, with the SVM model achieving the highest AUC; **B**. Demonstrates that the nomogram combining the SVM radscore with clinical features outperforms the radiomics model. AUC: Area under the curve; SVM: Support Vector Machine

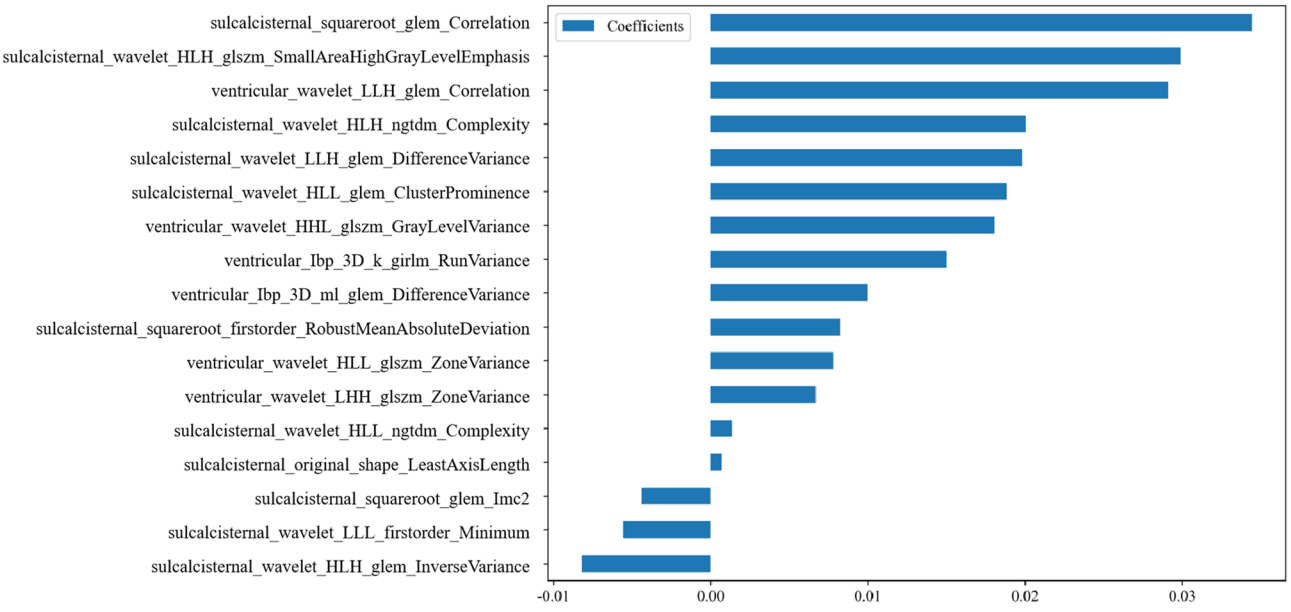


**Fig. 7** The radiomics features were selected through logistic regression and their corresponding weights

accumulation in the ventricles, which might contribute to disrupted fluid dynamics and DCI development. Together, these features enhance the model's ability to predict DCI by capturing diffuse and localized hemorrhage patterns.

The present study has certain advantages. Most of the existing studies for predicting DCI are purely clinical models or only use the feature of bleeding volume on images. This study is faster and more convenient using automatic segmentation + image histology feature analysis. Compared with current machine learning related studies, the required clinical features are easier to obtain and have better clinical generalization value. Despite the promising results, our study has several limitations. First, age differences between the DCI and non-DCI groups could have influenced the outcomes. Although t-tests showed significant age differences in both the training and validation cohorts, age was not identified as an independent factor in the multivariable analysis and, therefore, was not included in the

final nomogram. This may be due to the complex interactions between age and other clinical variables, which may have reduced its significance in a multivariable context. To address this limitation, future studies should consider larger sample sizes, stratified analyses, or age-matching techniques to better evaluate the impact of age on predictive performance. Second, the retrospective design and single-center methodology may introduce bias, our findings require validation in larger, multicenter, prospective studies. Third, while we achieved satisfactory predictive performance, the model was developed using a specific set of imaging parameters from three different CT scanners, potentially limiting its generalizability to other settings. Finally, the current work only analyzes the predictive performance of the imaging features of the hemorrhagic region for the onset of ischemia, and the addition of CTP reflecting perfusion of the whole brain may be able to improve the performance of the model, and future work should incorporate features such as perfusion metrics of CTP as well as external validation.

## Conclusions

In conclusion, this study successfully developed an NCCT-based radiomics nomogram that integrates radiomics features with clinical parameters including aneurysm location, treatment approach, and Hunt-Hess score, to predict DCI in aSAH patients. The model demonstrated high predictive performance and offers a valuable tool for early identification of high-risk patients.

## Supplementary Information

The online version contains supplementary material available at https://doi.org/10.1186/s12880-025-01722-0.

Supplementary Material 1

**Acknowledgements**
We thank National Natural Science Foundation of China and Capital's Funds for Health Improvement and Research for supporting the research.

**Author contributions**
Lingxu Chen was responsible for study design, model construction, and manuscript drafting. Xiaochen Wang reviewed the manuscript. Sihui Wang revised the manuscript. Xuening Zhao and Ying Yan conducted image analysis. Mengyuan Yuan performed literature review and data analysis. Shengjun Sun provided guidance, contributed to study design, and secured funding.

**Funding**
The research was funded by National Natural Science Foundation of China (82371939), National Natural Science Foundation of China (81971614) and Capital's Funds for Health Improvement and Research (2022-2-1074).

**Data availability**
The datasets used and/or analysed during the current study are available from the corresponding author on reasonable request.

## Declarations

**Ethics approval and consent to participate**
This study was conducted in accordance with the Declaration of Helsinki, and was approved by the Institutional Review Board (IRB) of Beijing Tiantan Hospital, Capital Medical University (KY2022-058-02). The IRB waived the need for informed consent forms.

**Consent for publication**
All the participants consented to the use of participant data for the study.

**Competing interests**
The authors declare no competing interests.

Received: 18 February 2025 / Accepted: 11 May 2025
Published online: 23 May 2025

**References**

1. Etminan N, Chang HS, Hackenberg K, et al. Worldwide incidence of aneurysmal subarachnoid hemorrhage according to region, time period, blood pressure, and smoking prevalence in the population: A systematic review and Meta-analysis. JAMA Neurol. 2019;76(5):588–97.
2. Claassen J, Park S. Spontaneous subarachnoid haemorrhage. Lancet. 2022;400(10355):846–62.
3. Neifert SN, Chapman EK, Martini ML, et al. Aneurysmal subarachnoid hemorrhage: the last decade. Transl Stroke Res. 2021;12(3):428–46.
4. Vergouwen MD, Vermeulen M, van Gijn J, et al. Definition of delayed cerebral ischemia after aneurysmal subarachnoid hemorrhage as an outcome event in clinical trials and observational studies: proposal of a multidisciplinary research group. Stroke. 2010;41(10):2391–5.
5. Galea JP, Dulhanty L, Patel HC. Predictors of outcome in aneurysmal subarachnoid hemorrhage patients: observations from a multicenter data set. Stroke. 2017;48(11):2958–63.
6. Dubosh NM, Bellolio MF, Rabinstein AA, et al. Sensitivity of early brain computed tomography to exclude aneurysmal subarachnoid hemorrhage: A systematic review and Meta-Analysis. Stroke. 2016;47(3):750–5.
7. Dupont SA, Wijdicks EF, Manno EM, et al. Prediction of angiographic vasospasm after aneurysmal subarachnoid hemorrhage: value of the Hijdra sum scoring system. Neurocrit Care. 2009;11(2):172–6.
8. Couret D, Boussen S, Cardoso D, et al. Comparison of scales for the evaluation of aneurysmal subarachnoid haemorrhage: a retrospective cohort study. Eur Radiol. 2024.
9. Frontera JA, Claassen J, Schmidt JM, et al. Prediction of symptomatic vasospasm after subarachnoid hemorrhage: the modified fisher scale. Neurosurgery. 2006;59(1):21–7. discussion 21–7.
10. Germans MR, Jaja B, de Oliviera Manoel AL, et al. Sex differences in delayed cerebral ischemia after subarachnoid hemorrhage. J Neurosurg. 2018;129(2):458–64.
11. de Rooij NK, Rinkel GJ, Dankbaar JW, et al. Delayed cerebral ischemia after subarachnoid hemorrhage: a systematic review of clinical, laboratory, and radiological predictors. Stroke. 2013;44(1):43–54.
12. Huang X, Wang D, Zhang Q, et al. Radiomics for prediction of intracerebral hemorrhage outcomes: A retrospective multicenter study. Neuroimage Clin. 2022;36:103242.
13. Yang L, Dong D, Fang M, et al. Can CT-based radiomics signature predict KRAS/NRAS/BRAF mutations in colorectal cancer. Eur Radiol. 2018;28(5):2058–67.
14. Yu F, Yang M, He C et al. CT radiomics combined with clinical and radiological factors predict hematoma expansion in hypertensive intracerebral hemorrhage. Eur Radiol 2024.
15. Zhang S, Gao L, Kang B, et al. Radiomics assessment of carotid intraplaque hemorrhage: detecting the vulnerable patients. Insights Imaging. 2022;13(1):200.
16. Shan D, Wang J, Qi P, et al. Non-Contrasted CT radiomics for SAH prognosis prediction. Bioeng (Basel). 2023;10(8):967.
17. Tong X, Feng X, Peng F, et al. Morphology-based radiomics signature: a novel determinant to identify multiple intracranial aneurysms rupture. Aging. 2021;13(9):13195–210.
18. Kohli M, Prevedello LM, Filice RW, et al. Implementing machine learning in radiology practice and research. AJR Am J Roentgenol. 2017;208(4):754–60.

19. Choy G, Khalilzadeh O, Michalski M, et al. Current applications and future impact of machine learning in radiology. Radiology. 2018;288(2):318–28.
20. Wichmann JL, Willemink MJ, De Cecco CN. Artificial intelligence and machine learning in radiology: current state and considerations for routine clinical implementation. Invest Radiol. 2020;55(9):619–27.
21. Martín Noguerol T, Paulano-Godino F, Martín-Valdivia MT, et al. Strengths, weaknesses, opportunities, and threats analysis of artificial intelligence and machine learning applications in radiology. J Am Coll Radiol. 2019;16(9 Pt B):1239–47.
22. Wang R, Dai W, Gong J, et al. Development of a novel combined nomogram model integrating deep learning-pathomics, radiomics and immunoscore to predict postoperative outcome of colorectal cancer lung metastasis patients. J Hematol Oncol. 2022;15(1):11.
23. Huang L, Lin W, Xie D, et al. Development and validation of a preoperative CT-based radiomic nomogram to predict pathology invasiveness in patients with a solitary pulmonary nodule: a machine learning approach, multicenter, diagnostic study. Eur Radiol. 2022;32(3):1983–96.
24. Christodoulou E, Ma J, Collins GS, Steyerberg EW, Verbakel JY, Van Calster B. A systematic review shows no performance benefit of machine learning over logistic regression for clinical prediction models. J Clin Epidemiol. 2019;110:12–22.
25. Zuo D, Yang L, Jin Y, Qi H, Liu Y, Ren L. Machine learning-based models for the prediction of breast cancer recurrence risk. BMC Med Inf Decis Mak. 2023;23(1):276.
26. Silva GFS, Fagundes TP, Teixeira BC, Chiavegatto Filho ADP. Machine learning for hypertension prediction: a systematic review. Curr Hypertens Rep. 2022;24(11):523–33.
27. Jin Y, Lan A, Dai Y, Jiang L, Liu S. Development and testing of a random forest-based machine learning model for predicting events among breast cancer patients with a poor response to neoadjuvant chemotherapy. Eur J Med Res. 2023;28(1):394.
28. Hao J, Luo S, Pan L. Rule extraction from biased random forest and fuzzy support vector machine for early diagnosis of diabetes. Sci Rep. 2022;12(1):9858.
29. Connolly ES Jr, Rabinstein AA, Carhuapoma JR, et al. Guidelines for the management of aneurysmal subarachnoid hemorrhage: a guideline for healthcare professionals from the American Heart Association/american Stroke Association. Stroke 2012;43(6):1711-37.
30. Neidert MC, Maldaner N, Stienen MN, et al. The Barrow neurological Institute grading scale as a predictor for delayed cerebral ischemia and outcome after aneurysmal subarachnoid hemorrhage: data from a nationwide patient registry (Swiss SOS). Neurosurgery. 2018;83(6):1286–93.
31. Zijlstra IA, Gathier CS, Boers AM, et al. Association of automatically quantified total blood volume after aneurysmal subarachnoid hemorrhage with delayed cerebral ischemia. AJNR Am J Neuroradiol. 2016;37(9):1588–93.
32. van der Steen WE, Zijlstra IA, Verbaan D, et al. Association of quantified Location-Specific blood volumes with delayed cerebral ischemia after aneurysmal subarachnoid hemorrhage. AJNR Am J Neuroradiol. 2018;39(6):1059–64.
33. Yuan JY, Chen Y, Jayaraman K, et al. Automated quantification of compartmental blood volumes enables prediction of delayed cerebral ischemia and outcomes after aneurysmal subarachnoid hemorrhage. World Neurosurg. 2023;170:e214–214222.
34. Huisman M, Akinci D, Antonoli T. What a radiologist needs to know about radiomics, standardization, and reproducibility. Radiology. 2024;310(2):e232459.
35. Le N. Hematoma expansion prediction: still navigating the intersection of deep learning and radiomics. Eur Radiol. 2024;34(5):2905–7.
36. Mukherjee S, Patra A, Khasawneh H, et al. Radiomics-based machine-learning models can detect pancreatic cancer on prediagnostic computed tomography scans at a substantial lead time before clinical diagnosis. Gastroenterology. 2022;163(5):1435-46.e3.
37. Ramos LA, van der Steen WE, Sales Barros R, et al. Machine learning improves prediction of delayed cerebral ischemia in patients with subarachnoid hemorrhage. J Neurointerv Surg. 2019;11(5):497–502.
38. Savarraj J, Hergenroeder GW, Zhu L, et al. Machine learning to predict delayed cerebral ischemia and outcomes in subarachnoid hemorrhage. Neurology. 2021;96(4):e553–553562.
39. de Jong G, Aquarius R, Sanaan B, et al. Prediction models in aneurysmal subarachnoid hemorrhage: forecasting clinical outcome with artificial intelligence. Neurosurgery. 2021;88(5):E427–427434.
40. Xiao ZK, Wang B, Liu J et al. Risk factors for the development of delayed cerebral ischemia after aneurysmal subarachnoid hemorrhage: A systematic review and meta-analysis. World Neurosurg 2024:S1878-8750(24)01653-01653X [pii].
41. Liu H, Xu Q, Li A. Nomogram for predicting delayed cerebral ischemia after aneurysmal subarachnoid hemorrhage in the Chinese population. J Stroke Cerebrovasc Dis. 2020;29(9):105005.
42. Göttsche J, Piffko A, Pantel TF, et al. Aneurysm location affects clinical course and mortality in patients with subarachnoid hemorrhage. Front Neurol. 2022;13:846066.


## Publisher's note